Supporting Information

Anthony et al. 10.1073/pnas.1115045109

SI Methods

RNA Sequences and Preparation. All sequences were derived from the wild-type thiamine pyrophosphate (TPP)-binding aptamer in the 3′ untranslated region of the *Arabidopsis thaliana thiC* gene (1) (GenBank accession code AC005496.3). Sense and antisense DNA oligonucleotides containing the full aptamer sequence (111 nt) or portions thereof, and flanked by 6 nt linkers (Fig. 1*A*), were custom-synthesized by IDT, annealed in STE buffer (100 mM NaCl, 10 mM Tris-HCl, 1 mM EDTA, pH 8.0), and cloned into the pALB3 plasmid at the unique BstEII restriction site. A portion of the plasmid was PCR-amplified in order to introduce a T7 promoter site upstream of the inserted sequence, and the RNA was synthesized by run-off in vitro transcription using the MEGAScript T7 kit (Ambion). All RNA was PCA-extracted, precipitated from isopropanol, and stored at ∼70 nM in STE buffer. The length and sequence of each ∼100–200 nt transcript was verified by RT-PCR.

Dumbbell Preparation. Each RNA molecule was measured as part of a molecular "dumbbell" (Fig. 1*B*) consisting of the RNA, two double-stranded DNA handles, and two polystyrene beads. Each handle included a single-stranded overhang complementary to one end of the RNA, and a chemical modification at the opposite end allowing the handle to bind specifically to one type of bead. A 2,018-bp handle with a 37-nt 5′ overhang and a digoxygenin label at the opposite end was prepared by PCR, using one aminosticky primer (2), one 5′-digoxygenin-modified primer, and the M13mp18 plasmid as the template. A 1,044-bp handle with a 31-nt 3′ overhang and a biotin label at the opposite end was prepared by PCR templated on the pALB3 plasmid, using one primer containing a phosphorothiote bond and one 5′-biotin-modified primer, followed by digestion with lambda exonuclease (3). All primers were obtained from IDT, and both handles were purified on spin columns. To assemble the dumbbell, the RNA was first annealed to the handles in STE buffer, with the RNA (∼20 nM) in up to ∼4-fold excess of each handle, by lowering the temperature from 80 to 4 °C over 30 min. The annealing mixture was then diluted 30- to 1,000-fold in phosphate buffer (100 mM sodium phosphate, 3 mg/mL BSA, pH 7.5) and added in an equal volume to 0.6 μm-diameter avidin-coated beads and 0.73 μm-diameter anti-digoxigenin-coated beads (each present at ∼50 pM in phosphate buffer). Incubation at room temperature for 1 h yielded dumbbells, which were diluted 1:20 in PHC buffer (50 mM Hepes, 130 mM KCl, 4 mM $MgCl_2$, 0.1 mM EDTA, 1 mM DTT, 0.1 mg/mL BSA) containing an oxygen-scavenging system (0.8% wt/vol β-D-glucose, 0.01 U/μL each of glucose-oxidase and catalase, Sigma), RNAse inhibitor (0.2 U/μL, Ambion), and any ligand such as TPP (Sigma). This mixture was micropipetted into a microscope flow-cell for measurement. Some constructs were also measured using PHC buffer containing 1 mM EDTA and lacking $MgCl_2$ (Fig. S1, Table S1).

Optical Trapping Instrumentation and Assay. All measurements were made with a dual-beam optical trapping microscope described previously (4, 5). Briefly, a ∼2 W, 1,064 nm YVO_4 trapping laser (Spectra-Physics) was split by polarization into two separate beam paths, which were passed through the objective of an inverted microscope (Nikon) and steered in the specimen plane using acousto-optical deflectors (AODs; IntraAction). The AODs were also used to modulate the intensity (stiffness) of the traps. In order to detect the positions of the trapped beads independently, a ∼10 mW 633 nm HeNe beam (Uniphase) was similarly delivered to the objective in two paths, each of which was coincident with one of the trapping beams and incident on a position-sensitive diode (PSD; Pacific Silicon Sensors) after the condenser. Trap stiffnesses were calibrated as described (6) by suspending beads in water and measuring Brownian fluctuations and associated Lorentzian roll-off frequencies in the position, and induced displacements under laminar flow. Computed stiffness values were reduced by ∼4% to correct for the difference in refractive index between the assay buffer and water. The temperature of the experimental room was maintained to within 0.2 °C, and the temperature at the sample was estimated to be 23 ± 0.5 °C.

The coverglass surface was searched for dumbbells using a three-dimensional (3D) piezoelectric microscope stage with a two-dimensional (2D) substage (Physik Instrumente), and candidate dumbbells were pulled from the surface into solution using the trapping beams. Selected beads were raster-scanned in tandem through the detecting beams in order to calibrate the position sensors for each dumbbell. Several force-extension curves (FECs) were obtained for each dumbbell prior to further measurements, and the initial portions of these curves were fitted by a worm-like chain interpolation formula (7). Dumbbells with low persistence lengths (<20 nm), which tended to have multiple tethers, were discarded. All experimental routines involving dumbbell manipulation and data acquisition were carried out using software custom-written in LabView (National Instruments). All data were sampled at 20 kHz and low-pass Bessel filtered online at 10 kHz.

Acquisition and Analysis of Nonequilibrium FECs with Hysteresis. FECs corresponding to increasing or decreasing extension (unfolding or refolding, respectively) were obtained by moving the traps in minute, evenly spaced steps at a constant ramp rate (∼60 nm/s). The same trap positions were used for both directions of each pulling cycle. The intensities of the two traps were modulated to provide roughly equal stiffnesses in each (0.2–0.3 pN/nm). Each data point represented 10 ms signal integration time. Trap motion was switched from increasing to decreasing extension when the measured force surpassed a threshold (e.g., 35 pN), and was paused for 1 s at the minimum extension (corresponding to ∼0 pN) between cycles. Most data for the WT aptamer in the absence of ligand were obtained at a high trap stepping rate (∼200 nm/s).

For each pulling cycle, an estimate of the rip force corresponding to ligand dissociation (or, in the case of FECs without apparent ligand dissociation events, the force of the first unfolding event) was made by automatically locating the extension at which the difference between the unfolding and refolding forces was maximal. If necessary, the location of the rip could be further adjusted by eye, and always corresponded to a local maximum in force.

The FECs for each molecule were aligned to remove the effect of small amounts of instrumental drift, using the following procedure, which is a variation of one described previously (8). First, each unfolding FEC was partitioned into three segments: a portion preceding the rip, corresponding to ligand dissociation ("prerip"), a portion after the last unfolding feature ("upper"), and the intervening portion. Next, a line was fit to the first ∼150 nm of extension of the aggregated prerip dataset, which corresponds primarily to stretching of the DNA handles. The slope obtained from this ensemble fit was used to constrain individual fits to the same segments of the prerip data, to obtain

individual force-offset values. Each unfolding FEC was then translated in force by an amount, typically <1 pN, equal to the difference between its individual offset and the ensemble average. This step has the effect of aligning each FEC in force to the average position of all FECs before the rip. Similarly, lines were fit to the aggregated data from the upper portions, this time to obtain an average extension offset. Each unfolding FEC was then translated in extension by an amount, typically <10 nm, equal to the difference between its individual offset and the ensemble average. This step aligned each FEC in extension to the average position of all FECs after the last unfolding feature. Finally, each refolding FEC was aligned to the corresponding unfolding FEC from the same cycle using an analogous method of fitting lines. The rip force for each FEC was then recalculated based on its aligned position. By removing systematic drift using this alignment procedure, we are able to determine the remaining variance in the rip-force distribution, which is due to stochasticity in the force required to dissociate the ligand.

As described previously (8), a function proposed by Dudko, et al. (9) was fitted to distributions of rip forces to parameterize the initial energy barrier to unfolding in terms of $\Delta G^{\ddagger}$ (the height of the barrier), $\Delta x^{\ddagger}$ (the distance to the barrier), and k_{off} (the intrinsic off-rate of any ligand). The input parameter, ν, was alternately set to $\frac{1}{2}$ or $\frac{2}{3}$, corresponding to a cusp-like or linear-cubic potential, respectively, and results were pooled and averaged for both parameter values. Trap ramp rates were ~60 nm/s and ~200 nm/s, corresponded to loading rates of 5–10 pN/s and 18–20 pN/s, respectively, at the rip. The rip-force distributions, $p(F_R)$, were also fitted using a function proposed by Maitra and Arya (10) that assumes a linear-cubic potential and is parameterized in terms of the stiffness of the trap (K) and the persistence length (P) and contour length (L) of the DNA handles:

$$p(F_R) \propto \frac{k(F_R)}{\dot{F}(F_R)} \exp\left\{ -\int_0^{F_R} \frac{k(F)}{\dot{F}(F)} \mathrm{d}F \right\},$$

where

$$\dot{F}(F) = V\left(\frac{(\Delta x^{\ddagger})^2}{6\Delta G^{\ddagger}} + \frac{2\beta LP(1+\beta FP)}{3+5\beta FP+8(\beta FP)^{2.5}} + \frac{1}{K} \right)^{-1},$$

$$k(F) = k_{\text{off}} \left(\chi^2 - \frac{2F\chi\Delta x^{\ddagger}}{3\Delta G^{\ddagger}} \right)^{\frac{1}{2}} \exp\left(\beta\Delta G^{\ddagger} \left\{ 1 - \left(\chi^2 - \frac{2F\chi\Delta x^{\ddagger}}{3\Delta G^{\ddagger}} \right)^{\frac{3}{2}} \right\} \right),$$

and

$$\chi = 1 + \frac{K(\Delta x^{\ddagger})^2}{6\Delta G^{\ddagger}}.$$

Here, $\beta = (k_{\text{B}}T)^{-1}$ and V is the trap speed. For both fitting functions, input parameters were constrained to the average values for all rips represented in the distribution. Distributions representing all pulls from each molecule were fitted individually, and the aggregate distribution for each apatmer/ligand condition (e.g., WT plus 2 mM TPP) was fitted separately. Results for per-molecule and aggregate fitting generally did not differ; both are presented in Table S2.

To obtain the P and L parameters, a single worm-like chain function was fitted to the prerip portion of each unfolding FEC using the modified Marko-Siggia interpolation formula (11). The upper portion, representing the stretching of both dsDNA handles and the unfolded RNA, was then modeled as the sum of two worm-like chains (WLCs), with the parameters for the first WLC constrained to those from the fit to the prerip portion, and assuming for the second WLC a ssRNA persistence length (12) of 1 nm and elastic modulus (13) of 1600 pN/nm. The contour length of the unfolded RNA, a parameter returned by the fit to the upper portion of the unfolding FEC, was used to determine the total number of nucleotides released as follows. The width of an A-form helix (14), 2.2 nm, was added to the measured contour length to account for the finite width of the RNA along the pulling axis prior to unfolding, and the result was divided by an RNA interphosphate distance of 0.59 nm/nt (14), corresponding to 3′-endo sugar pucker.

Equilibrium free energies changes for unfolding the aptamer and dissociating any bound ligand were calculated from nonequilibrium data using the methods developed by Bennett (15) and Collin, et al. (16–18). Each unfolding or refolding FEC was numerically integrated from the extension at zero force to the extension corresponding to the beginning of the upper portion. The integral of the double-WLC fit over the same domain was subtracted from these integrals to yield the work expended (or recovered) by the instrument to unfold (or refold) the system. (We note that because the double-WLC fitting was performed on each unfolding FEC individually, the alignment procedure described above did not affect the work calculated for unfolding, but did ensure that the work calculated for refolding in the same pulling cycle was not distorted due to drift.) Work histograms for the unfolding and refolding processes were compiled for all pairs of FECs measured for each molecule, and also aggregated for each aptamer/ligand condition. The equilibrium free energy is approximately given by the point of intersection of the unfolding and refolding histograms, but the values we report were determined rigorously, using the maximum-likelihood estimator developed by Shirts, et al. (19).

Constant-Force Measurements at Equilibrium. Repeated unfolding and refolding of individual RNA helices at constant force was observed by lowering the intensity of one trap to roughly one-third that of the other, then pulling the bead in the weak trap ~100–300 nm from the trap center. In this configuration, changes in molecular extension resulting from folding transitions cause only small perturbations to the force measured in the strong trap, so that the force is passively clamped. In particular, when a bead is in the "zero-stiffness region" (ZSR) of the weak trap (displaced ~240–290 nm from the trap center in our instrument), the intrinsic distance changes and rates of folding are distorted minimally by the compliance of the DNA handles and can be measured directly (20). All transitions were measured this way, but we found that transitions occurring at forces below ~13 pN were well-resolved only if significant positive stiffness existed in the weak trap. In such cases, we also carried out "open-loop" measurements with the bead in the weak trap displaced ~100–200 nm from the trap center, and corrected the measured distance changes and rates accordingly (20).

Folding transitions in the full aptamer constructs were initially identified by monitoring the molecular extension while lowering the force (via the intensity of the weak trap) gradually from ~25 to ~5 pN. Transitions in both the aptamer and helix constructs were then measured individually by lowering the force in smaller steps over the 2–3 pN range separating the fully unfolded from fully folded states. Time-series data for the force, extension, and displacement of the bead from the weak trap were acquired over consecutive 10 s windows, and the force was typically stepped every one or two windows. As the force was lowered across the transition, the molecule was observed to sample both the unfolded and folded states, spending an increasing amount of time in the folded state.

Each folding transition was analyzed as a two-state system using methods previously described (5, 8). The extension record for each force step was median-smoothed over a 10 ms interval and partitioned into two or three states (three when two transitions were poorly differentiated by force). A histogram of extensions was then constructed for each of these states and fitted by a

Gaussian function. The distance between the Gaussian peaks provided an estimate of Δx, the opening distance for the transition, and the relative areas of the histograms determined the fractional amount of time spent by the molecule in each state. The value of Δx reported for the molecule was the average Δx calculated for all force steps. $F_{1/2}$, the force at which the molecule spent equal time in the folded and unfolded states, was determined by plotting the fraction unfolded (or folded) vs. force and fitting a Boltzmann function for a two-state system (12): $P_U(F) = 1 + \exp[(F_{1/2} - F)\Delta x/k_BT]$, where $P_F(F) = 1 - P_U(F)$. The free energy change of unfolding, ΔG, was computed from $\Delta x \cdot F_{1/2}$, less the energy for stretching the newly unfolded ssRNA, determined by integrating a WLC function. Plots of $\ln(k_F)$ vs. force (where k_F is the average force-dependent transition rate) were linear, consistent with a sharp energy barrier ($k_F = k_0 \exp(F \cdot \Delta x^{\ddagger}/k_BT)$), and permitting calculation of the distance to the transition state ($\Delta x^{\ddagger}$) from both the folded and unfolded states from the slopes of linear fits (21). The point of intersection of the two fits for a transition provided an estimate of $k_{1/2}$, the average rate of transition at $F_{1/2}$.

Together, these parameters comprise a signature for each transition that can be compared among the various molecules and constructs (Table S1). The identities of the folding transitions were assigned by correlating the presence or absence of transitions in each construct with the presence or absence of sequence elements. Each helix generally produced a very similar signature in all the constructs where its folding was observed, with the exception of P1, as discussed in the main text.

The numbers of nucleotides released upon unfolding for each transition were calculated as $\Delta n = (\Delta x - 2.2 \cdot \Delta h)/D_b$, where D_b is the extension of ssRNA (nm/nt) at $F_{1/2}$ and Δh is the change in number of exposed helices. D_b was determined from the modified Marko-Siggia interpolation formula, again assuming a persistence length of 1 nm and an interphosphate distance of 0.59 nm/nt. The $2.2 \cdot \Delta h$ term accounts for the fact that an A-form RNA helix has a finite width (2.2 nm) which is included in the measured extension prior to unfolding, so that the quantity $\Delta x/D_b$ underestimates the number of nucleotides released upon unfolding a simple hairpin. However, if the helix leads to a junction from which h other helices stem, then $2h$ nucleotides will not be immediately stretched out but will instead together subtend $h \cdot 2.2$ nm, a greater distance. We chose $\Delta h = -1$ for the P3high and P5 transitions, $\Delta h = 0$ for P2, P3low, and P4, and $\Delta h = +1$ for P1.

Folding Energy Landscapes. The energy landscapes of the WT, A105G, and A90G aptamers (Fig. 2) in the absence of ligand were reconstructed as described (8) from constant-force data to illustrate the energetics of unfolding the helices in succession. In brief, the ΔG values (inclusive of the ssRNA stretching energy) for each folding transition were added cumulatively, in the order of increasing $F_{1/2}$ values, to establish the energies of the folding states. The distances between the states, and from each state to the adjacent transition state(s), were set by the Δx and $\Delta x^{\ddagger}$ values, respectively. The heights of the barriers between states were determined from $\Delta G^{\ddagger} = -k_BT \cdot \ln(k_{1/2}/k_0)$, where $k_0 = 10^5\ s^{-1}$ is a drag-dependent prefactor determined previously (5). Each reconstructed landscape was then tilted to a given force (e.g., $F = 8$ pN) by subtracting $F \cdot x$, where x is the cumulative extension relative to the fully folded state. The P3low transition was not observed directly in any of the aptamers in constant-force measurements: its contribution was inferred from data pooled from the P3 and P2/3 constructs.

Ligand binding to the WT and A90G aptamers caused reversible folding of the P1 and P2 helices to be too slow to characterize at constant force, but did not appear to perturb the folding energetics of the other helices. We therefore used measurements of the global folding and unfolding of the aptamers (described above) to characterize the ligand-induced stabilization of the fully folded state, and the resulting perturbation of the energy landscapes. The difference in ΔG values, determined by analysis of the mechanical work of folding in the presence or absence of ligand, provided the decrease in free energy for the fully folded state, depicted in Fig. 2 (inset). The ΔG value for the WT aptamer in the absence of ligand was used as the benchmark for the stabilization of A90G by TPP, because FECs were not measured for the bare A90G aptamer, and the sum of the helix energies of the WT and A90G aptamers differed by <1%. The heights and locations of the energy barriers for ligand dissociation were provided by an analysis of rip-force distributions using the method of Dudko (9). Here, landscape parameters ($\Delta G^{\ddagger}$, $\Delta x^{\ddagger}$) were determined for all pulls performed on each molecule and then averaged across molecules.

Analysis of TPP Binding Kinetics. The kinetics of TPP binding to the WT aptamer were characterized by measuring FECs of aptamer molecules while varying the TPP concentration and the lag time between pulling cycles. In contrast to experiments involving hysteretic FECs described above, only FECs resulting from increasing the molecular extension were recorded. Here, the traps were moved in stepwise increments eightfold larger (resulting in ramp loading rates of ~60–80 pN/s at TPP-dependent rips), and the traps were restored within ~10 ms to their starting positions, corresponding to ~0 pN, when the maximum-force threshold was surpassed.

The FECs from each dataset (comprising a subset of the measurements made at a single TPP concentration and refolding time) were superimposed for inspection (but not aligned), and the presence or absence of a TPP-dependent rip in each FEC was determined by eye. The average force for the P3high transition in FECs lacking TPP-dependent rips (~18 pN) was used as a threshold for classifying TPP-dependent rips as being either high-force or low-force. The initial FEC for each dataset was discarded, because the amount of time for which the aptamer was held at zero force prior to measurement was poorly controlled. Similarly, FECs that appeared unusually short and lacked both TPP-dependent rips and helix unfolding transitions were discarded: these likely resulted from TPP being bound to the aptamer throughout the measurement and not dissociating before the maximum force was reached.

For each TPP concentration, at least five aptamer molecules were measured and 1,600 FECs were acquired. The data in Fig. 4 represent a total of 12,781 FECs acquired from a total of 45 molecules, and were globally fit by a four-state kinetic model containing two TPP-bound states. We distinguished between the binding states in our measurements based on the rip force (with F′-TPP and F″-TPP corresponding to low- and high-force TPP-dependent rips, respectively), suggesting that TPP binding becomes tighter with time. Standard binomial errors were incorporated in the global fitting and uncertainties in the rate constants. We corroborated the asymptotic behavior of the trends plotted in Fig. 4 by measuring one aptamer molecule at 5 μM TPP with a 100 s refolding time, observing a TPP-dependent rip in 78 out of 99 FECs (79 ± 4%), of which 74 (95 ± 2%) occurred at high-force. The "dead time" of each pulling cycle, defined as the time taken for the force to increase from 0 to 8 pN ($F_{1/2}$ value for the P1 helix), was approximately 0.8 s, and this amount was added to the refolding time at each point before performing the global fitting.

Error Analysis. The two primary sources of systematic error in these experiments were in the measured distances that beads were displaced from the optical trap center, and in the measured forces. Uncertainties in displacement were largely due to uncertainty in the absolute distance calibration of the PSDs, and were estimated at 2%. The uncertainties in distance changes measured

at constant force, however, were somewhat larger (~5%) due to uncertainty in the location of the ZSR of the weak trap, which affects how measured values scaled relative to their true molecular values (20). Uncertainties in force arise from variability in the sizes of beads, used both for stiffness calibration and measurement, as well as from fluctuations in the intensities of the trapping beams, which can occur on a time scale of weeks to months. We calibrated the trap stiffnesses approximately monthly, using ~6–10 beads, and estimate the systematic error in force at about 5%. Additional uncertainty existed in the temperature of the sample and in the change in stiffness due to substituting buffer for water in the flow-cell, and these factors together contributed another ~1% to the overall uncertainty in force. Finally, we estimate a systematic uncertainty of 0.1 in the values of $\ln(k_{1/2})$ determined from analysis of constant-force data, reflecting the sensitivity of these values to changing the width of the median-smoothing window by ~50%.

The uncertainties depicted in Fig. 2, as well as those reported in the Tables S1 and S2, represent the statistical standard errors of the mean added in quadrature to the estimated systematic errors.

1. Sudarsan N, Barrick JE, Breaker RR (2003) Metabolite-binding RNA domains are present in the genes of eukaryotes. *RNA* 9:644–647.
2. Gal J, Schnell R, Szekeres S, Kalman M (1999) Directional cloning of native PCR products with preformed sticky ends (autosticky PCR). *Mol Gen Genet* 260:569–573.
3. Spitzer S, Eckstein F (1988) Inhibition of deoxyribonucleases by phosphorothioate groups in oligodeoxyribonucleotides. *Nucleic Acids Res* 16:11691–11704.
4. Woodside MT, et al. (2006) Direct measurement of the full, sequence-dependent folding landscape of a nucleic acid. *Science* 314:1001–1004.
5. Woodside MT, et al. (2006) Nanomechanical measurements of the sequence-dependent folding landscapes of single nucleic acid hairpins. *Proc Natl Acad Sci USA* 103:6190–6195.
6. Neuman KC, Block SM (2004) Optical trapping. *Rev Sci Instrum* 75:2787–2809.
7. Bustamante C, Marko JF, Siggia ED, Smith S (1994) Entropic elasticity of lambda-phage DNA. *Science* 265:1599–1600.
8. Greenleaf WJ, Frieda KL, Foster DA, Woodside MT, Block SM (2008) Direct observation of hierarchical folding in single riboswitch aptamers. *Science* 319:630–633.
9. Dudko OK, Hummer G, Szabo A (2006) Intrinsic rates and activation free energies from single-molecule pulling experiments. *Phys Rev Lett* 96:108101.
10. Maitra A, Arya G (2011) Influence of pulling handles and device stiffness in single-molecule force spectroscopy. *Phys Chem Chem Phys* 13:1836–1842.
11. Wang MD, Yin H, Landick R, Gelles J, Block SM (1997) Stretching DNA with optical tweezers. *Biophys J* 72:1335–1346.
12. Liphardt J, Onoa B, Smith SB, Tinoco IJ, Bustamante C (2001) Reversible unfolding of single RNA molecules by mechanical force. *Science* 292:733–737.
13. Seol Y, Skinner GM, Visscher K (2004) Elastic properties of a single-stranded charged homopolymeric ribonucleotide. *Phys Rev Lett* 93:118102.
14. Saenger W (1984) *Principles of Nucleic Acid Structure* (Springer-Verlag, New York).
15. Bennett CH (1976) Efficient estimation of free-energy differences from Monte-Carlo data. *J Comput Phys* 22:245–268.
16. Collin D, et al. (2005) Verification of the Crooks fluctuation theorem and recovery of RNA folding free energies. *Nature* 437:231–234.
17. Crooks GE (1999) Entropy production fluctuation theorem and the nonequilibrium work relation for free energy differences. *Phys Rev E* 60:2721–2726.
18. Crooks GE (2000) Path-ensemble averages in systems driven far from equilibrium. *Phys Rev E* 61:2361–2366.
19. Shirts MR, Bair E, Hooker G, Pande VS (2003) Equilibrium free energies from nonequilibrium measurements using maximum-likelihood methods. *Phys Rev Lett* 91:140601.
20. Greenleaf WJ, Woodside MT, Abbondanzieri EA, Block SM (2005) Passive all-optical force-clamp for high-resolution laser trapping. *Phys Rev Lett* 95:208102.
21. Bustamante C, Chemla YR, Forde NR, Izhaky D (2004) Mechanical processes in biochemistry. *Annu Rev Biochem* 73:705–748.

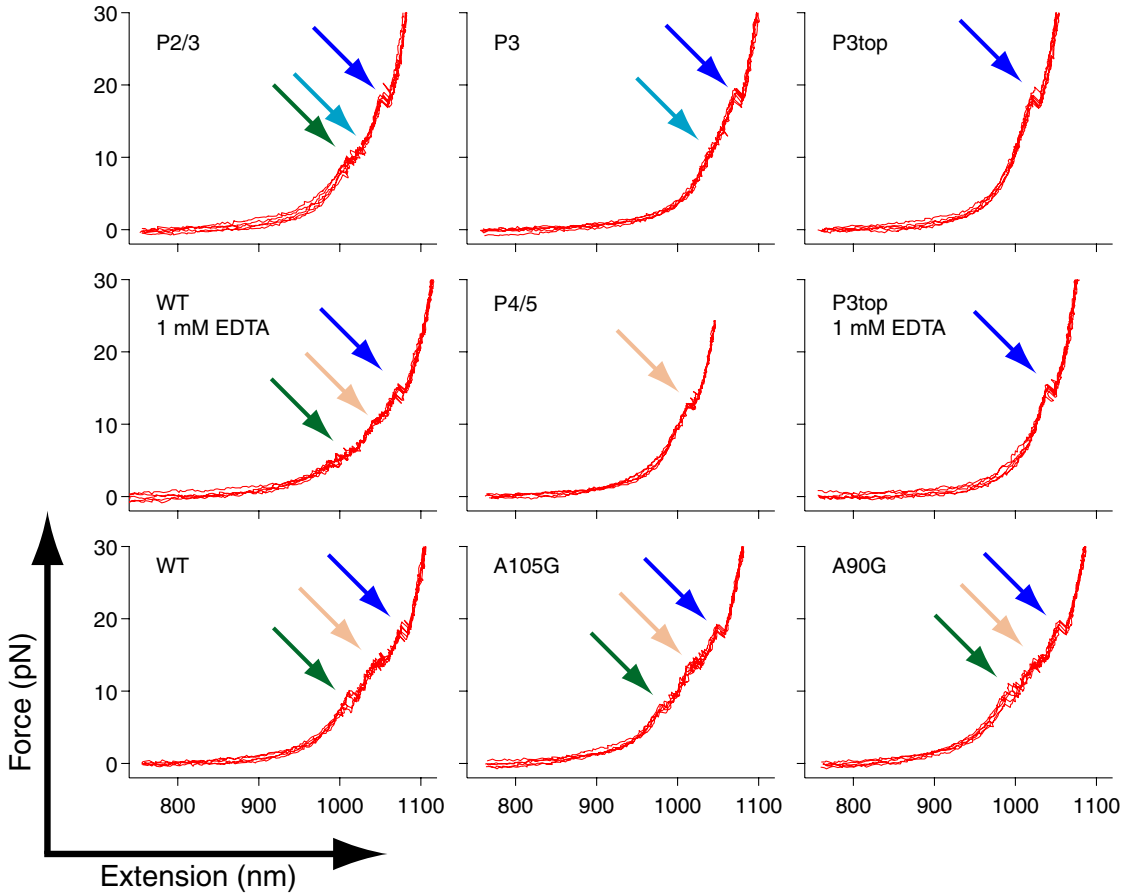

Fig. S1. Gallery of FECs for full-length and truncated aptamer constructs. Each graph displays five FECs performed on a representative molecule for the designated construct (legend inset). Data were acquired in standard buffer (*SI Methods*) unless otherwise noted. Unfolding transitions are indicated (colored arrows): P3high (dark blue), P3low (light blue), P4 and P5 (pink), P1 and/or P2 (green). The P3low transition was not directly observed in constant-force measurements of the full aptamer constructs.

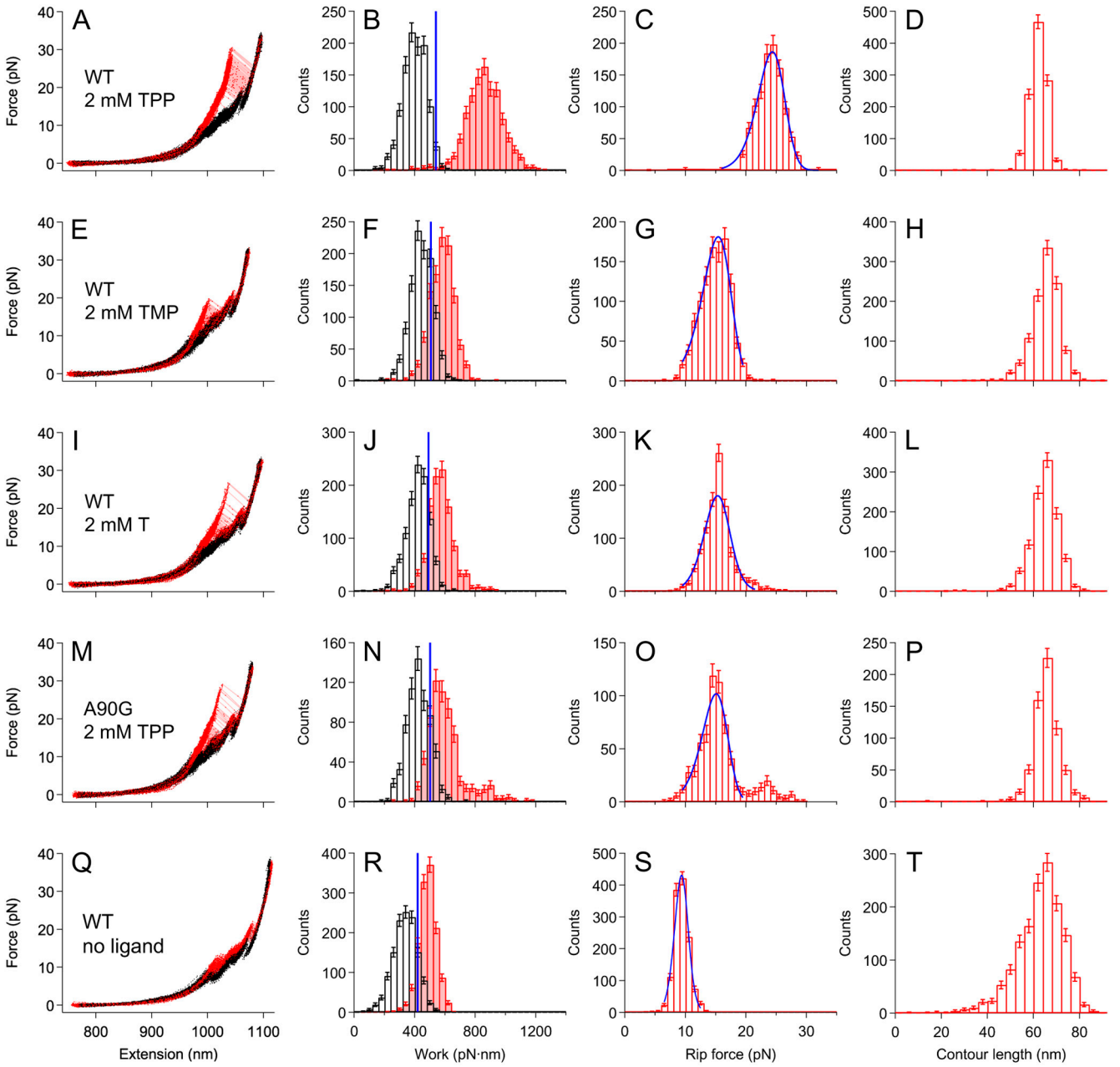

Fig. S2. Analysis of hysteretic *F-x* data for the WT and A90G aptamers in the presence or absence of ligand. For each set of conditions tested (shown on separate rows), a total of ~1,000 reversible folding cycles were measured from 5–7 aptamer molecules (Table S2): (*A*–*D*) WT in the presence of 2 mM TPP, (*E*–*H*) WT in the presence of 2 mM TMP, (*I*–*L*) WT in the presence of 2 mM T, (*M*–*P*) A90G in the presence of 2 mM TPP, (*Q*–*T*) WT in the absence of ligand. Graphs in the first column (*A*, *E*, *I*, *M*, *Q*) display FECs (150 cycles) for unfolding (red) and refolding (black) a representative molecule. Graphs in subsequent columns reflect analysis of FECs obtained from all folding cycles, aggregated across molecules. The second column (*B*, *F*, *J*, *N*, *R*) displays histograms (mean ± s.e.) for the work of unfolding (red) and refolding (black) the construct. Free energy changes (blue lines) for unfolding and ligand dissociation (where applicable) were calculated using Bennett's Acceptance Ratio (BAR) (1, 2). The third column (*C*, *G*, *K*, *O*, *S*) displays histograms (mean ± s.e.) of the unfolding rip forces, fitted using Dudko's function (3) (blue curves), assuming $\nu = \frac{1}{2}$: the fits supply the energetic and kinetic parameters $\Delta x^{\ddagger}$, $\Delta G^{\ddagger}$, and k_{off}. The fourth column (*D*, *H*, *L*, *P*, *T*) displays histograms (mean ± s.e.) of the total change in contour length, a proxy for the number of nucleotides released upon unfolding, obtained from WLC fits to FECs (*SI Methods*). A numerical summary is presented in Table S2. WT molecules were measured in the absence of ligand at two loading rates (~5–10 pN/s and ~18–20 pN/s); the data shown here are for the faster loading rate (1,291 cycles, 5 molecules).

1 Bennett CH (1976) Efficient estimation of free-energy differences from Monte-Carlo data. *J Comp Phys* 22:245–268.
2 Shirts MR, Bair E, Hooker G, Pande VS (2003) Equilibrium free energies from nonequilibrium measurements using maximum-likelihood methods. *Phys Rev Lett* 91:140601.
3 Dudko OK, Hummer G, Szabo A (2006) Intrinsic rates and activation free energies from single-molecule pulling experiments. *Physical Review Letters* 96:108101.

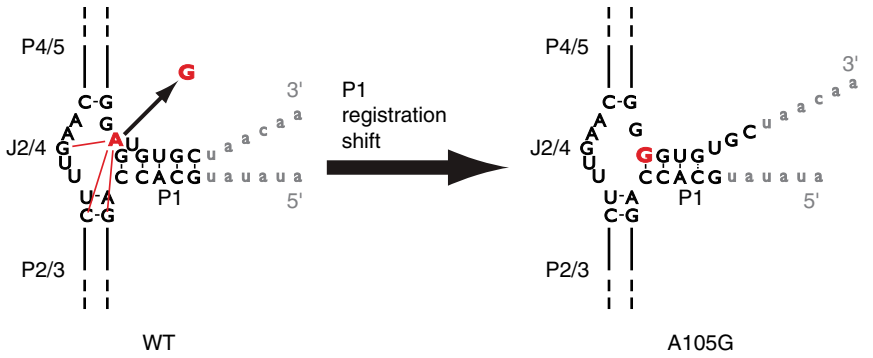

Fig. S3. Proposed change in P1 helix pairing for the A105G mutant aptamer. The extension change associated with the P1 transition in the A105G mutant aptamer was 2.2 ± 0.6 nm smaller than that of the WT aptamer, corresponding to the pairing of 6 ± 2 fewer nt. The difference is explained by a change in the registration of the 5′ and 3′ strands of the helix, which is predicted by *mfold* (1), and the consequent fraying of the P1 helix. Transitions in the two aptamers were roughly isoenergetic, consistent with the bulged U107 residue in the WT aptamer forming no significant contacts with the P1 helix or other parts of the aptamer (2). The steric strain imposed upon the P1 helix by U107 is relieved by the mutation, thereby offsetting the loss of enthalpic stabilization from several base-pairs.

1 Zuker M (2003) Mfold web server for nucleic acid folding and hybridization prediction. *Nucleic Acids Res* 31:3406–3415.
2 Thore S, Leibundgut M, Ban N (2006) Structure of the eukaryotic thiamine pyrophosphate riboswitch with its regulatory ligand. *Science* 312:1208–1211.

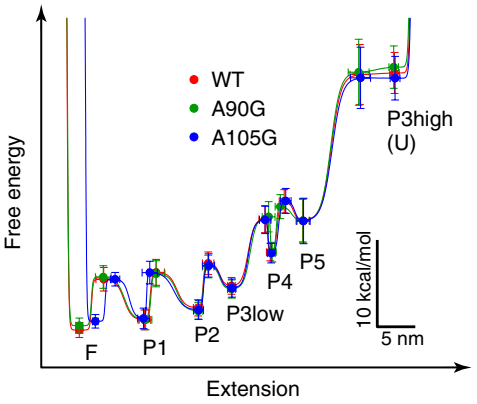

Fig. S4. Comparison of energy landscapes for the WT and mutant aptamers in the absence of ligand. Energy landscapes were aligned by eye; all landscapes are shown tilted by the work done by 8 pN of applied force. The contributions to all three landscapes from the P3low transition were inferred from data acquired from the P2/3 and P3 constructs. (All states and labels are identical to those in Fig. 2, main text.)

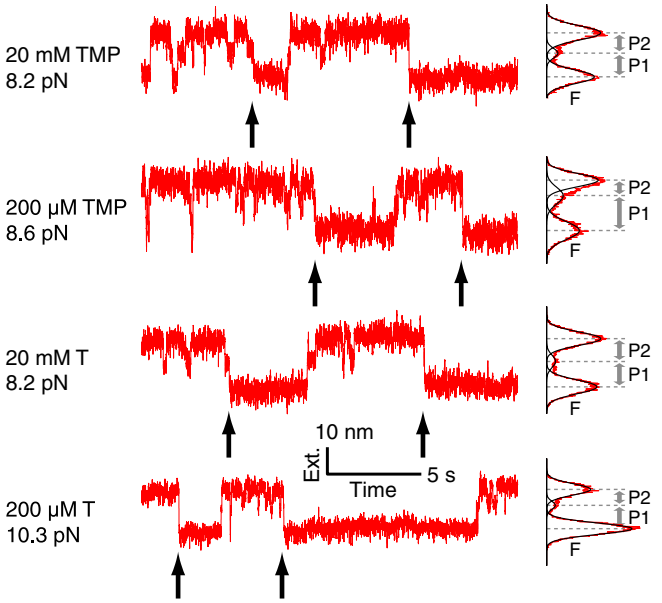

Fig. S5. Transient binding of TMP and T to the WT aptamer. *Left*, records of extension vs. time for P1 and P2 folding under constant forces (as indicated) for aptamers in the presence of ligand, showing presumed ligand binding events (black arrows). Signals were acquired in a passive force-clamp configuration (rather than open-loop), and therefore the data are noisier (and distance changes larger) than those shown in Fig. 3 (main text). *Right*, histograms of extension and Gaussian fits, with peaks labeled as in Fig. 1*D*.

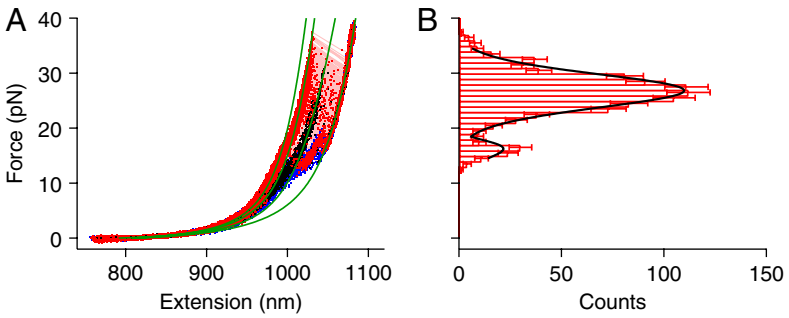

Fig. S6. Varied unfolding behavior in a single WT aptamer molecule. (*A*) 1,211 FECs were obtained from a single aptamer molecule in the presence of 2 mM TPP under a maximum loading rate of ~40 pN/s. The traps were restored to their initial positions as quickly as possible once the maximum force was reached; data were recorded only during extension, and a refolding time of 2 s was imposed between cycles. No TPP-dependent rip was observed in 226 (19%) of cases (blue). For all other FECs, separate WLC functions (green) were fitted to the data below 8 pN (far left) and to the higher-force data where all structure had been removed (far right). These fits yielded an unfolding distance of 63 ± 3 nm, corresponding to 110 ± 6 nt. For 32 FECs (3% of the total; black), unfolding and TPP dissociation proceeded through an intermediate, corresponding to the unfolding of 24 ± 4 nt, i.e., to the approximate combined lengths of the P1 and P2 helix stems plus the nucleotides in the J2/4 junction. All 953 remaining FECs displayed a TPP-dependent rip (red). Here, the data above 19 pN (if any) were fitted separately, yielding an additional extension of 11 ± 1 nt relative to the folded structure, corresponding to the approximate length of the unfolded P1 helix stem. Note that no partial unfolding prior to the TPP-dependent rip was observed at lower pulling speeds (Fig. 3). (*B*) Histogram (mean $\pm$ s.e.) of all TPP-dependent rip forces in (*A*). The two peaks were fitted separately using the formalism of Dudko, et al. (*SI Methods*), using both $\nu = \frac{1}{2}$ (fits shown) and $\nu = \frac{2}{3}$. We obtained averaged results of $\Delta G^{\ddagger} = 11 \pm 1$ kcal/mol, $\Delta x_f^{\ddagger} = 3.8 \pm 0.4$ nm, $\ln(k_{off}) = -11 \pm 3\ s^{-1}$ for the low-force peak and $\Delta G^{\ddagger} = 15 \pm 1$ kcal/mol, $\Delta x_f^{\ddagger} = 4.0 \pm 0.6$ nm, $\ln(k_{off}) = -20 \pm 1\ s^{-1}$ for the high-force peak.

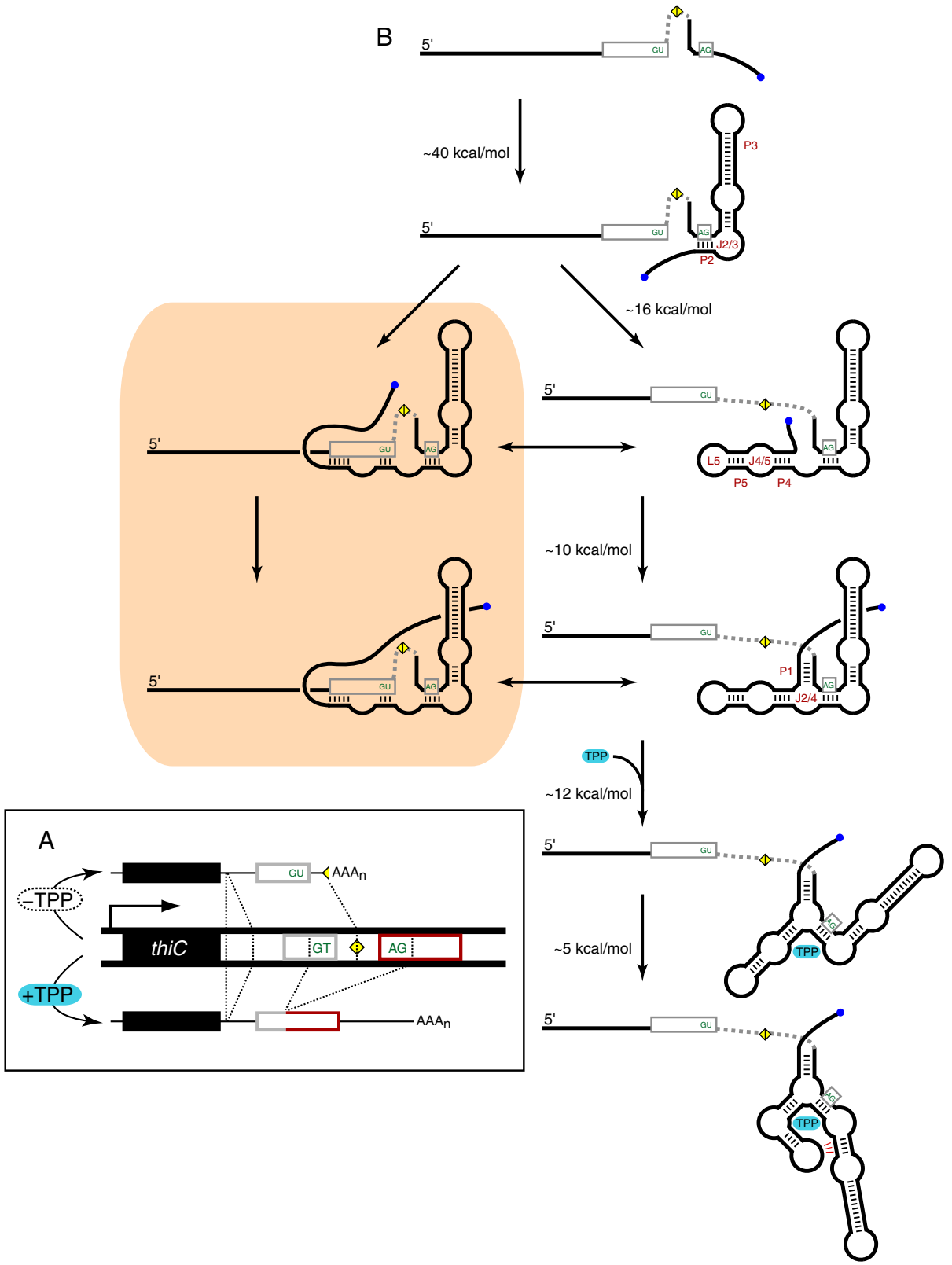

Fig. S7. A cotranscriptional view of aptamer folding and the TPP riboswitch mechanism in *A. thaliana*. (*A*) Overview of TPP riboswitch-mediated processing of *thiC* 3′ UTR, as elucidated previously (1, 2). *Center*, simplified illustration (not to scale) of key DNA sequence elements downstream of the *thiC* gene. The TPP aptamer (red rectangle) is situated ~400 bp downstream of the *thiC* ORF (black rectangle) and carries a 3′ splice site (AG) in the P2 helix. The corresponding 5′ splice site (GT) is contained within an 8 bp tract (gray rectangle), located ~150 bp upstream of the aptamer, which is complementary to the 5′ strand of the P4/5 helix arm. A transcript-processing site (yellow diamond), at which the transcript can be cut and polyadenylated, occurs between these two splice sites. *Top and bottom*, processed *thiC* transcripts. TPP binding is thought to disrupt base-pairing between the aptamer and the 5′ splice site, rendering the site more accessible and allowing splicing to proceed (2). This disruption results in processing-site excision and yields a longer, less stable final transcript. Both types of transcript are made shorter by excision of a 182 nt intron beginning 3 nt downstream of the *thiC* stop codon. (*B*) Conjectural model of cotranscriptional folding in the 3′ UTR.

Transcription progresses from top to bottom. Each blue dot represents the 3′ end of the RNA emerging from the RNA polymerase. Elements of secondary structure not present in the previous state(s) are labeled, and the energies (measured in the present study) to form these structures or to bind TPP are indicated. [*N.B*: Because we studied the isolated aptamer, these energies do not reflect TPP-dependent structural changes (2) associated with ~150 nt sequence located between the 5′ splice site and aptamer (dashed gray line)].

Our data indicate that TPP binding to the aptamer requires folding of the P1 helix and the proper arrangement of J2/4. In splicing-incompetent configurations of the 3′ UTR (shaded), it is unlikely that both of these requirements are met. Furthermore, the native fold of the P4/5 helix arm, which binds the pyrophosphate moiety of TPP, is disrupted [mutations in J4/5 have been shown to reduce TPP binding to the *E. coli thiM* aptamer (3)]. Therefore, these configurations are deemed unlikely to bind TPP, and TPP binding to the aptamer does not directly break interactions between the P4/5 helix arm and the 5′ splice site. These observations suggest that an opportunity exists to form the shorter transcript (*A*, top) from splicing-incompetent configurations of the 3′ UTR even at high TPP concentrations. Switch efficiency likely depends upon the relative stabilities of the splicing-competent and splicing-incompetent configurations, and the rates of interconversion between these.

1 Bocobza S, et al. (2007) Riboswitch-dependent gene regulation and its evolution in the plant kingdom. *Genes Dev* 21:2874–2879.
2 Wachter A, et al. (2007) Riboswitch control of gene expression in plants by splicing and alternative 3′ end processing of mRNAs. *Plant Cell* 19:3437–3450.
3 Ontiveros-Palacios N, et al. (2008) Molecular basis of gene regulation by the THI-box riboswitch. *Mol Microbiol* 67:793–803.

Table S1. Summary of constant-force data

Construct/conditions	Folding trans.	*N*	Δx (nm)	Δx (nt)	$F_{1/2}$ (pN)	$\ln(k_{1/2})(s^{-1})$	$\Delta G^{\ddagger}$ (kcal/mol)	$\Delta x_f^{\ddagger}$ (nm)	$\Delta x_u^{\ddagger}$ (nm)
WT	P3high	12	12.1 ± 0.6	32 ± 2	17.8 ± 1.0	0.9 ± 0.1	6.2 ± 0.1	5.9 ± 0.4	3.6 ± 0.3
	P5	12	4.3 ± 0.2	15 ± 1	13.9 ± 0.8	4.2 ± 0.1	4.3 ± 0.1	1.9 ± 0.3	2.3 ± 0.2
	P4	12	5.1 ± 0.3	12 ± 1	13.3 ± 0.8	4.2 ± 0.1	4.3 ± 0.1	3.3 ± 0.3	0.6 ± 0.1
	P2	6	7.0 ± 0.4	19 ± 1	9.4 ± 0.5	2.7 ± 0.2	5.2 ± 0.1	1.5 ± 0.4	4.9 ± 0.5
	P1	6	8.5 ± 0.4	17 ± 1	8.9 ± 0.5	2.3 ± 0.3	5.4 ± 0.2	1.3 ± 0.2	2.4 ± 0.6
WT, 2 μM TPP	P3high	8	11.9 ± 0.6	32 ± 2	17.3 ± 1.0	1.0 ± 0.1	6.2 ± 0.1	6.8 ± 0.6	3.9 ± 0.3
	P5	7	4.2 ± 0.2	15 ± 1	13.8 ± 1.0	4.2 ± 0.1	4.3 ± 0.1	1.5 ± 0.2	2.6 ± 0.2
	P4	7	5.0 ± 0.3	12 ± 1	13.2 ± 0.9	4.1 ± 0.1	4.4 ± 0.1	3.9 ± 0.3	0.7 ± 0.1
WT, 1 mM EDTA	P3high	5	11.4 ± 0.6	32 ± 1	14.5 ± 0.9	1.5 ± 0.2	5.9 ± 0.1	6.8 ± 0.6	5.0 ± 0.3
A105G	P3high	8	12.0 ± 0.6	32 ± 2	17.5 ± 1.1	0.9 ± 0.1	6.3 ± 0.1	6.3 ± 0.4	3.9 ± 0.3
	P5	8	4.3 ± 0.2	15 ± 1	14.1 ± 0.9	4.1 ± 0.1	4.3 ± 0.1	2.2 ± 0.5	2.4 ± 0.2
	P4	8	5.2 ± 0.3	12 ± 1	13.4 ± 0.9	4.0 ± 0.2	4.4 ± 0.1	3.4 ± 0.2	0.6 ± 0.1
	P2	4	7.2 ± 0.4	19 ± 1	8.9 ± 0.7	2.7 ± 0.2	5.2 ± 0.1	0.7 ± 0.2	5.5 ± 0.3
	P1	4	6.3 ± 0.4	11 ± 1	8.4 ± 0.7	3.5 ± 0.2	4.7 ± 0.1	2.1 ± 0.5	3.0 ± 0.5
A105G, 2 mM TPP	P2	3	7.3 ± 0.4	20 ± 1	8.7 ± 0.7	2.8 ± 0.2	5.1 ± 0.1	0.7 ± 0.3	5.5 ± 0.3
	P1	3	6.4 ± 0.3	12 ± 1	8.1 ± 0.7	3.5 ± 0.2	4.7 ± 0.1	2.2 ± 0.3	2.3 ± 0.4
A90G	P3high	7	11.9 ± 0.6	31 ± 2	18.3 ± 1.0	1.0 ± 0.1	6.2 ± 0.1	6.0 ± 0.5	4.1 ± 0.9
	P5	5	4.0 ± 0.2	15 ± 1	14.2 ± 0.9	4.2 ± 0.1	4.3 ± 0.1	0.9 ± 0.2	2.3 ± 0.2
	P4	5	5.3 ± 0.3	13 ± 1	13.5 ± 0.9	4.0 ± 0.2	4.4 ± 0.1	3.6 ± 0.4	0.4 ± 0.1
	P2	5	6.9 ± 0.4	18 ± 1	9.0 ± 0.6	2.9 ± 0.2	5.1 ± 0.1	1.5 ± 0.6	5.2 ± 0.9
	P1	5	8.7 ± 0.4	18 ± 1	8.5 ± 0.5	2.4 ± 0.3	5.3 ± 0.2	1.6 ± 0.4	2.5 ± 0.2
A90G, 2 μM TPP	P3high	3	11.9 ± 0.6	31 ± 2	18.7 ± 1.0	1.1 ± 0.1	6.1 ± 0.1	6.5 ± 0.5	3.4 ± 0.4
	P5	2	4.1 ± 0.4	15 ± 2	14.6 ± 0.8	4.2 ± 0.1	4.3 ± 0.1	1.5 ± 0.4	2.5 ± 0.7
	P4	2	5.3 ± 0.3	13 ± 1	13.8 ± 0.7	4.0 ± 0.1	4.4 ± 0.1	3.3 ± 0.8	0.5 ± 0.2
P3	P3high	9	12.0 ± 0.6	32 ± 2	17.7 ± 1.0	1.0 ± 0.2	6.2 ± 0.1	5.7 ± 0.4	3.7 ± 0.3
	P3low	6	4.3 ± 0.2	11 ± 1	11.5 ± 0.7	4.2 ± 0.2	4.3 ± 0.1	2.7 ± 0.3	4.6 ± 0.4
P3top	P3high	7	11.4 ± 0.6	30 ± 2	17.9 ± 0.9	1.0 ± 0.1	6.2 ± 0.1	5.5 ± 0.4	3.8 ± 0.3
P3top, 1 mM EDTA	P3high	7	11.0 ± 0.6	30 ± 2	15.7 ± 0.9	1.5 ± 0.1	5.9 ± 0.1	6.2 ± 0.4	3.9 ± 0.3
P2/3	P3high	10	12.1 ± 0.6	32 ± 2	17.4 ± 1.0	0.9 ± 0.1	6.3 ± 0.1	6.6 ± 0.5	3.6 ± 0.3
	P3low	6	4.5 ± 0.2	11 ± 1	12.5 ± 0.7	4.1 ± 0.1	4.4 ± 0.1	1.8 ± 0.3	5.3 ± 0.3
	P2	6	8.4 ± 0.4	21 ± 1	10.4 ± 0.6	2.3 ± 0.2	5.4 ± 0.1	2.4 ± 0.2	3.7 ± 0.4
P4/5	P5	6	4.1 ± 0.2	15 ± 1	13.0 ± 0.8	4.2 ± 0.1	4.3 ± 0.1	1.7 ± 0.2	3.0 ± 0.2
	P4	6	4.8 ± 0.3	12 ± 1	12.4 ± 0.7	4.2 ± 0.1	4.3 ± 0.1	3.9 ± 0.4	0.9 ± 0.2

N, the number of molecules measured. Values represent mean ± uncertainty, computed from the standard error added in quadrature to estimated systematic errors (*SI Methods*).

Table S2. Summary of hysteretic force-extension data

Construct/ conditions	*N*	Total pulls	Contour length (nm)	nt released	BAR ΔG (kcal/mol)	$\Delta G^{\ddagger}$ (kcal/mol)	$\Delta x_f^{\ddagger}$ (nm)	$\Delta x_f^{\ddagger}$ (nt)	$\ln(k_{off})$ (s^{-1})
WT, 2 mM TPP	5	1,091	**62 ± 3**	**109 ± 6**	**78 ± 4**	**15 ± 3**	**4 ± 2**	**12 ± 5**	**−21 ± 4**
			62 ± 4	*109 ± 6*	*80 ± 5*	*15 ± 1*	*4.5 ± 0.4*	*12 ± 1*	*−22 ± 1*
						15 ± 1	**4.3 ± 0.2**	**12 ± 1**	**−21 ± 1**
						15 ± 1	*4.4 ± 0.2*	*12 ± 1*	*−21 ± 1*
WT, 2 mM TMP	7	1,086	**65 ± 4**	**114 ± 6**	**73 ± 4**	**7.7 ± 0.5**	**3.2 ± 0.4**	**9 ± 1**	**−9 ± 1**
			64 ± 4	*112 ± 6*	*72 ± 6*	*8 ± 1*	*3.3 ± 0.3*	*9 ± 1*	*−9 ± 1*
						8.2 ± 0.4	**3.3 ± 0.2**	**9 ± 1**	**−9 ± 1**
						8.0 ± 0.4	*3.4 ± 0.2*	*9 ± 1*	*−9 ± 1*
WT, 2 mM T	6	1,071	**65 ± 4**	**113 ± 6**	**71 ± 4**	**10 ± 1**	**5 ± 2**	**12 ± 4**	**−12 ± 3**
			65 ± 4	*113 ± 6*	*72 ± 4*	*10 ± 1*	*4.1 ± 0.3*	*11 ± 1*	*−12 ± 1*
						9 ± 1	**3.3 ± 0.2**	**9 ± 1**	**−9 ± 1**
						9 ± 1	*3.4 ± 0.3*	*9 ± 1*	*−10 ± 1*
A90G, 2 mM TPP	5	651	**66 ± 4**	**115 ± 6**	**72 ± 4**	**9 ± 1**	**4 ± 1**	**10 ± 2**	**−10 ± 1**
			65 ± 4	*114 ± 6*	*71 ± 4*	*10 ± 1*	*3.3 ± 0.4*	*9 ± 1*	*−10 ± 1*
						10 ± 1	**3.1 ± 0.2**	**8 ± 1**	**−9 ± 1**
						9 ± 1	*3.5 ± 0.2*	*9 ± 1*	*−10 ± 1*
WT, no ligand	7	1,476	**62 ± 3**	**109 ± 6**	**61 ± 3**	**12 ± 1**	**12 ± 3**	**31 ± 8**	**−15 ± 3**
			59 ± 4	*104 ± 7*	*60 ± 4*	*11 ± 1*	*10 ± 1*	*27 ± 2*	*−13 ± 1*
						N.D.	N.D.	N.D.	N.D.

N, the number of molecules measured. Data were analyzed both in the aggregate (**bold**) and by molecule (*italics*). Reported values represent mean (or best estimate) ± uncertainty, computed from the statistical error added in quadrature to estimated systematic errors (*SI Methods*). For aggregated datasets, the statistical error is the standard error of the mean (for *contour length, nt released*), the variance of the maximum-likelihood estimator (for BAR ΔG), or the parameter error returned from curve fits ($\Delta x_f^{\ddagger}$, $\Delta G^{\ddagger}$, ln k_{off}). For data analyzed by molecule, the statistical error is standard error of the mean. The parameters $\Delta x_f^{\ddagger}$, $\Delta G^{\ddagger}$, and ln k_{off} were calculated using the methods of both Dudko (1) and Maitra (2) (top and bottom of each cell, respectively).

1 Dudko OK, Hummer G, Szabo A (2006) Intrinsic rates and activation free energies from single-molecule pulling experiments. *Phys Rev Lett* 96:108101.
2 Maitra A, Arya G (2011) Influence of pulling handles and device stiffness in single-molecule force spectroscopy. *Phys Chem Chem Phys* 13:1836–1842.